Classical and Quantum Gravity

PAPER

OPEN ACCESS

RECEIVED
13 July 2025

REVISED
20 November 2025

ACCEPTED FOR PUBLICATION
5 December 2025

PUBLISHED
18 December 2025

An integrated fiber phase modulation device for optical path noise suppression

Juan Wang[1], **Keqi Qi**[1], **Heshan Liu**[1], **Pan Li**[1], **Ruihong Gao**[1], **Shaoxin Wang**[1,*] and **Ziren Luo**[1,2]

[1] Center for Gravitational Wave Experiment, Key Laboratory of Microgravity, Institute of Mechanics, Chinese Academy of Sciences, Beijing, People's Republic of China
[2] School of Fundamental Physics and Mathematical Sciences, Hangzhou Institute for Advanced Study, Chinese Academy of Sciences, Hangzhou, People's Republic of China
[*] Author to whom any correspondence should be addressed.

E-mail: wangshaoxin@imech.ac.cn

Keywords: fiber phase modulation, optical path difference noise, AOM sideband noise

Abstract

This paper presents an integrated fiber phase modulation device (FPMD) to suppress front-end optical path difference (OPD) noise in heterodyne interferometry systems, particularly addressing noise induced by acoustic-optic modulator sideband coupling. To achieve real-time optical path stabilization, the FPMD employs a polarization-maintaining fiber coupled with piezoelectric ceramics in a monolithic aluminum structure. The compact, all-fiber design offers enhanced immunity to environmental disturbances while simplifying integration into precision interferometric systems. Through systematic characterization, the FPMD exhibits a highly linear response (270.5949 nm V^{-1}, $R^2 = 0.99914$) and effective noise suppression in the critical sub-10 mHz frequency band, achieving picometer-level ranging accuracy across the entire frequency band above 2 mHz. This work provides a theoretical framework and experimental validation for a robust solution to OPD noise in ultra-high-precision metrology applications.

1. Introduction

The space-based gravitational wave detection project detects gravitational wave signals by precisely monitoring the distance between two free-floating test masses [1–3]. Achieving the required ranging precision requires laser interferometry systems capable of picometer-level displacement measurement accuracy in the millihertz frequency band [4–6]. Heterodyne interferometers, serving as the primary measurement tool for test mass positioning on optical benches, typically employ hydroxide catalysis bonding technology and ultra-low thermal expansion materials to minimize optical noise [7–9]. However, when measurement precision surpasses the mrad (nm) level, the influence of front-end optical path noise in the system can no longer be neglected [10, 11].

The front-end optical path difference (OPD) noise primarily originates from electromagnetic crosstalk within the acoustic-optic modulator (AOM) drive signal [5, 12]. Sidebands in the AOM drive signal introduce additional beat frequency components into the interference signal, generating OPD noise that degrades the phase measurement accuracy of the interferometer [10, 12]. The stray light originating from AOM frequency coupling can introduce a phase error to interferometric phase measurement [13]. Two principal approaches exist for mitigating the impact of OPD noise and improving measurement precision in the low-frequency mHz band [5]: (1) enhancing the spectral purity of the AOM drive signal by reducing sideband amplitudes through optimization of the AOM driver circuit to minimize electromagnetic interference, or through employing low-noise RF signal sources and power amplifiers to suppress spurious frequency components; (2) establishing a coupling model between sideband-induced OPD noise and front-end OPD noise, followed by implementing either post-processing algorithms [14] or real-time dynamic optical path compensation to compensate for sideband-induced OPD fluctuations [12, 15]. The method for real-time dynamic optical path compensation requires a

feedback control loop to regulate the optical path. This method can reduce the design and manufacturing requirements for AOM driving circuits, while maintaining adaptability to environmental variations such as temperature fluctuations and mechanical vibrations. Additionally, it is worth noting that integrated acousto-optic platforms, such as those based on silicon photonics [16], may offer inherent advantages in reducing such electromagnetic crosstalk. However, the focus of the present study remains primarily on mitigating noise in conventional bulk AOM systems.

The adjustment of the front-end optical path can be implemented by employing a piezo-electric transducer (PZT) as the actuator. This configuration establishes a mechanical linkage between the mirror (or optical fiber) in the modulated optical path and the piezoelectric ceramic. Through precise voltage regulation in a feedback control system, the optical path length can be actively adjusted to compensate for OPD fluctuations caused by AOM sideband noise and other disturbances, thereby improving interferometric measurement accuracy [17]. Compared to reflector position control, fiber-coupled PZT offers superior precision while eliminating assembly and alignment errors. Currently, in the field of front-end OPD noise suppression, the optical fiber is directly wrapped and glued around the cylindrical surface of PZT [7, 12]. However, this method leaves the fiber highly susceptible to external environmental influences, and uneven adhesion can cause non-uniform deformation in the fiber, compromising the device's response accuracy. To address these limitations, this paper presents an integrated high-sensitivity fiber phase modulation device (FPMD) and evaluates its performance and OPD noise suppression capabilities.

To systematically address the aforementioned challenges, this paper is structured as follows: section 2 establishes the theoretical model of OPD noise induced by sideband coupling in AOM; section 3 details the design and implementation of a novel FPMD for active optical path compensation; section 4 validates the device's performance and demonstrates its effect in noise suppression through experimental characterization; finally, conclusions are drawn in section 5, highlighting the device's capability for picometer-level ranging accuracy.

2. Principle of OPD noise suppression

In the laser heterodyne interferometry optical path shown in figure 1, the two frequency-shifted beams generated by the AOMs are guided into the optical platform through collimators and are directed into the detector after passing through a series of optical components, enabling the acquisition of heterodyne interference signals. They are ultimately post-processed in the phasemeter (P.M.) for phase extracting [18, 19].

Taking the reference interferometer as an example, the two beams entering the detector can be expressed as:

$$E_1(t) = \cos\left[(\omega_0 + \omega_m)t + k\cdot(L_1 + L_{1R})\right],$$

$$E_2(t) = \cos\left(\omega_0 t + k\cdot(L_2 + L_{2R})\right),$$

where ω_m is the differential frequency of the two beams. k Is the wavenumber. L_1 And L_2 are the front-end optical path lengths. L_{1R} And L_{2R} represent the optical path length of the reference interferometer on the optical bench.

To demonstrate the effect of sidebands on interferometric phase, we consider the representative case where beam E2 includes an extra sideband, as follows:

$$\mathrm{E}_2(t) = \cos\left(\omega_0 t + k\cdot(L_2 + L_{2R})\right) + \varepsilon\cdot\cos\left[(\omega_0 + \omega_s)t + k\cdot(L_2 + L_{2R})\right],$$

where ε and ω_s are the amplitude and frequency of the sideband signal, respectively. The interference signal in the reference detector is

$$I(t) = |E_1(t) + E_2(t)|^2.$$

Taking the second-order sideband ($\omega_s = +2\omega_m$) as an example, the ω_m —frequency components of the interference signal can be expressed as:

$$I_{\omega_m} \propto \cos(\omega_m t + \Delta F + \Delta R) + \varepsilon\cdot\cos(\omega_m t - \Delta F - \Delta R).$$

where Δ denotes the optical path phase difference. $\Delta F = k\cdot(L_1 - L_2)$ Denotes the front-end OPD, and $\Delta R = k\cdot(L_{1R} - L_{2R})$ for that in the reference interferometer.

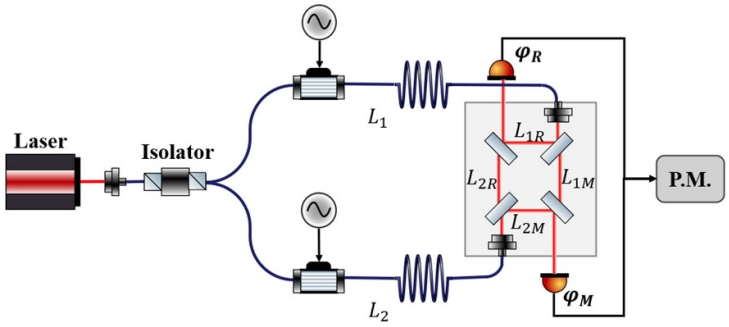

Figure 1. Schematic diagram of a heterodyne interferometer.

Table 1. The phase errors for different sideband frequencies.

ω_s	$\delta\varphi$
$+2\omega_m$	$2\varepsilon\cdot\cos(2\Delta F+\Delta M+\Delta R)\cdot\sin(\Delta M-\Delta R)$
$+\omega_m$	$2\varepsilon\cdot\cos\left(\Delta F+\frac{\Delta M+\Delta R}{2}\right)\cdot\sin\left(\frac{\Delta M-\Delta R}{2}\right)$
$-\omega_m$	$2\varepsilon\cdot\cos\left(\Delta F+\frac{\Delta M+\Delta R}{2}\right)\cdot\sin\left(\frac{\Delta M-\Delta R}{2}\right)$
$-2\omega_m$	0

The phase of the reference interferometer can be extracted as

$$\varphi_R=\arctan\left(\frac{I_{\omega_m}\cdot\cos(\omega_m t)}{I_{\omega_m}\cdot\sin(\omega_m t)}\right)\approx\Delta F+\Delta R-\varepsilon\cdot\sin(2\Delta F+2\Delta R).$$

Similarly, the phase of the measurement interferometer is:

$$\varphi_M\approx\Delta F+\Delta M-\varepsilon\cdot\sin(2\Delta F+2\Delta M).$$

Therefore, the final differential phase of the two interferometers can be calculated as

$$\begin{aligned}\varphi&=\varphi_R-\varphi_M\\&=\Delta M-\Delta R-2\varepsilon\cdot\cos(2\Delta F+\Delta M+\Delta R)\cdot\sin(\Delta M-\Delta R).\end{aligned}$$

Thus, the phase error can be expressed as:

$$\begin{aligned}\delta\varphi&=\varphi-(\Delta M-\Delta R)\\&=2\varepsilon\cdot\cos(2\Delta F+\Delta M+\Delta R)\cdot\sin(\Delta M-\Delta R).\end{aligned}$$

The expression demonstrates that the differential phase is not only related to the disturbance of the optical bench but also varies with twice of ΔF in a trigonometric functional relationship, which is caused by the cross-coupling between the two AOMs.

When different sideband couplings in the optical beam are considered, the resulting phase errors vary. Based on the above analysis, the phase error results corresponding to the different sidebands in beam E2 are summarized in table 1. A more comprehensive derivation can be found in [12]. As evidenced, phase measurement errors in the interference signals are correlated with fluctuations in the front-end optical path.

To eliminate the influence of external disturbances on the front-end optical path and improve interferometric measurement accuracy, the adjustable optical fiber can be introduced into the front-end optical path to lock the ΔF at a specific value. This approach can be implemented by coupling the optical fiber with PZT, whereby the fiber length is precisely adjusted through voltage control of the PZT, thereby achieving front-end optical path stabilization.

3. Implementation of FPMD

To achieve precise control of the front-end optical path variation, i.e. ΔF, an integrated high-sensitivity FPMD is developed, with its schematic and physical diagrams shown in figures 2 and 3.

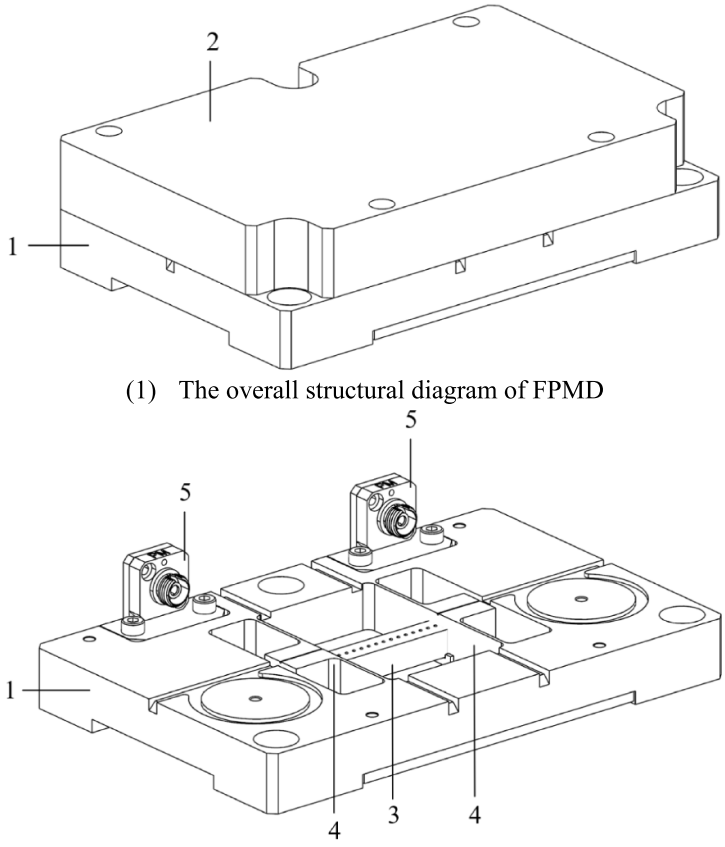

Figure 2. Schematic diagrams of FPMD. (1: Main body; 2: enclosure; 3: PZT; 4: *T*-shaped platform; 5: fiber optic mating sleeves).

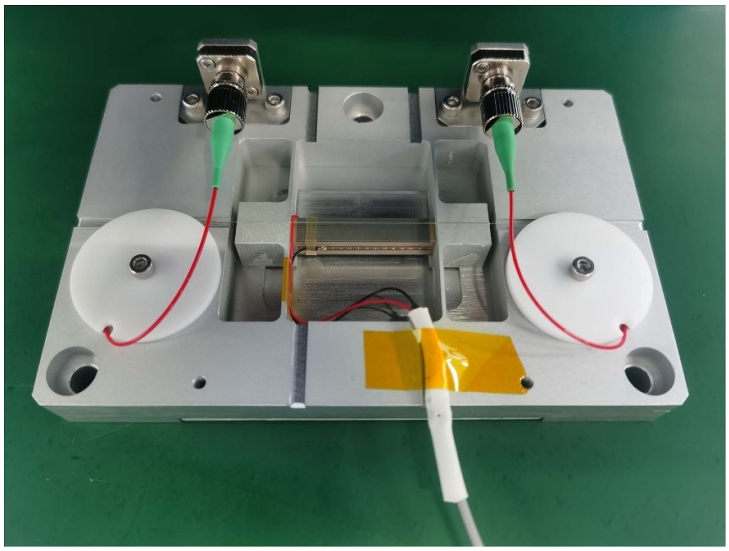

Figure 3. Physical diagrams of FPMD.

A polarization-maintaining optical fiber is encapsulated within the device, with a specific segment coupled to PZT. This configuration enables real-time dynamic feedback compensation of front-end OPD noise by actively adjusting the sensitive fiber segment's length through PZT voltage modulation.

The device primarily consists of three core components: the main body, optical fiber, and PZT.

The main body is fabricated from monolithic aluminum, featuring some precision-machined surface grooves designed for several functions, such as mounting of fiber optic mating sleeves, routing of optical fiber paths, positioning of PZT, and organized channeling of PZT power supply wiring. For example,

two T-shaped platforms are integrated at the central section of the main body for fiber guiding and PZT positioning. The transverse arms of the T-shaped platforms are monolithically fabricated with the main body, while the longitudinal arms feature head-end clearances. Semi-circular grooves are precision-machined along the fiber routing direction on the upper surfaces for fiber adhesive bonding. To isolate the optical fiber from environmental disturbance, the upper surface of the main body is sealed by the housing enclosure.

The optical fiber, serving as the core component for front-end optical path adjustment, is integrated into the system via two fiber optic mating sleeves. Within the device, the fiber is routed through two circular fiber grooves with a horizontal middle section traversing both T-shaped platforms. The fiber segments on the upper surface of the T-shaped platform are adhesively bonded, while the intermediate section remains suspended.

The optical path adjustment of the optical fiber is realized by the PZT. The PZT is positioned between the transverse arms of the two T-shaped platforms, and the bottom of the PZT is secured by clamping grooves. Both end faces are adhesively bonded to the T-shaped platform. The electrodes are attached to the front and rear surfaces of PZT, with associated wires routed externally to the PZT controller for real-time voltage regulation, as shown in figure 3.

4. Performance test and noise suppression of FPMD

4.1. Performance test of FPMD

To characterize the response of FPMD, an optical path was configured as shown in figure 4. One FPMD is integrated into one arm of the heterodyne interferometer. Its driving voltage, controlled by a PZT amplifier, can be adjusted to change the front-end path length fluctuation. To characterize the intrinsic response of FPMD, the optical fiber displacement measurement noise caused by path length fluctuation is recorded. Two signals are ultimately input to the P.M. for phase extracting:

1) 1 MHz reference signal (φ_0) derived from the AOM driving signals through frequency mixing and low-pass filtering.
2) Reference interferometric signal (φ_R).

The phase difference $\varphi_R - \varphi_0$ reflects the OPD fluctuation of the measurement system. It is dominated by the front-end OPD (ΔF) fluctuations, as the interferometer optical platform is more stable than the front-end modulated optical path.

In one experimental set, the PZT amplifier's output voltage was incremented from 10 V in 0.1 V steps at 1 s intervals until reaching 24.3 V. The phase difference of the interferometric signal measured by P.M. yielded the corresponding displacement measuring information as follows:

$$\Delta s = \frac{\varphi_R - \varphi_0}{2\pi}\lambda.$$

The result of the performance test is shown in figure 5.

It demonstrates that the displacement result exhibits a stepwise increase, where each step corresponds to a change in the PZT amplifier's output voltage (indicated by black arrows). For coupling coefficient calibration, the coupling coefficient was extracted by analyzing an 80 s dataset, where the displacement noise at each voltage level was evaluated using five randomly sampled data points, as displayed in the inset. Based on this dataset, the relationship between displacement noise and voltage of the PZT amplifier is shown in figure 6.

The resulting error bars represent the mean values with standard deviations as error margins. The minimal error bar magnitude indicates low measurement noise, demonstrating the high precision performance of FPMD.

Besides, the fitting curve between displacement noise y (nm) and voltage of PZT amplifier x (V) is:

$$y = 270.5949 * x - 3003.5285$$

with goodness-of-fitting of:

$$R^2 = 0.999\,14.$$

Thus, we have determined the OPD response coefficient of the FPMD as 270.5949 nm V^{-1}, confirming the linear relationship between applied voltage and optical path length variation in the device control process.

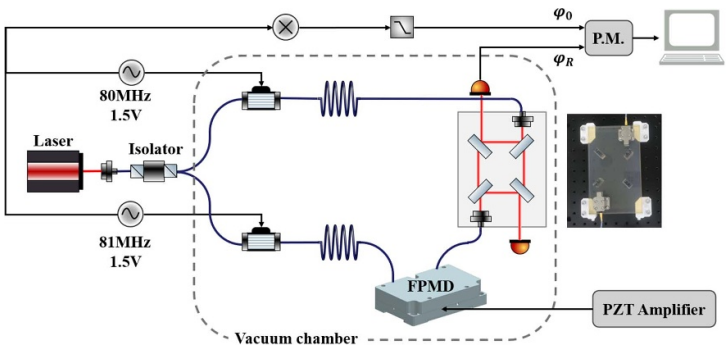

Figure 4. The optical path diagram for a performance test of FPMD.

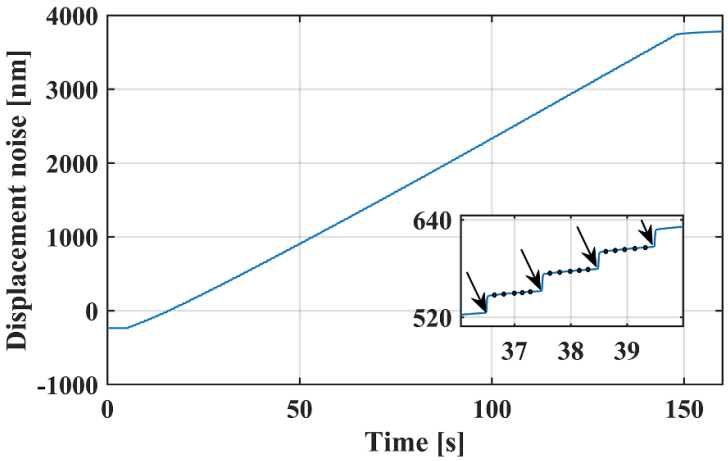

Figure 5. The displacement response for FPMD voltage adjustment.

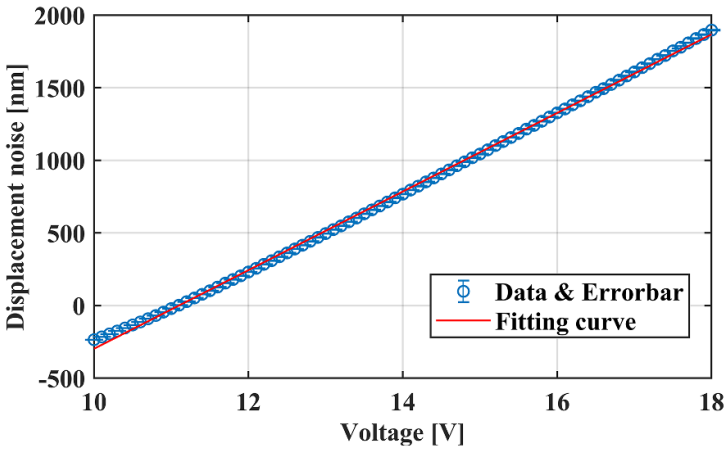

Figure 6. The displacement response fitting curve for FPMD.

4.2. Interference signal response to OPD fluctuation

Subtracting the two interference signals can, in principle, suppress common-mode noise [20, 21]. The effect of the front-end OPD is expected to be eliminated by this method. However, as derived theoretically above, the subtraction result remains correlated with the front-end OPD. It is therefore necessary to examine the relationship between the detected displacement measurement result ($\varphi_R - \varphi_M$) and the front-end OPD fluctuation. The optical path is characterized by the experimental setup in figure 7. Two FPMDs, powered by PZT amplifiers, are totally the same in design, so that the equal beam interferometry is guaranteed to decrease the laser frequency noise [7, 22, 23].

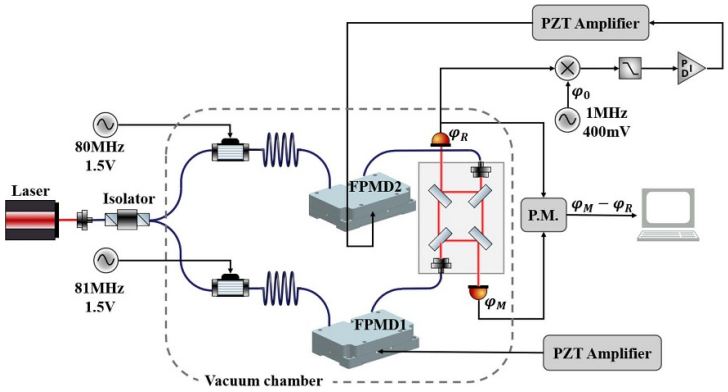

Figure 7. The optical path diagram for OPD noise suppression.

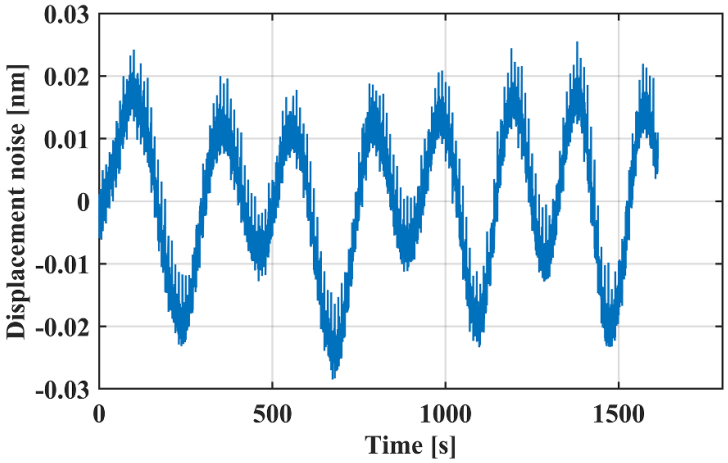

Figure 8. The displacement noise responses to OPD fluctuation.

During this procedure, the voltage of FPMD1 is incremented from 10 V in 0.1 V steps at 10 s intervals. To realize common-mode noise suppression, the displacement measurement result ($\varphi_R - \varphi_M$) is processed in P.M. and shown in figure 8.

It can be observed that the displacement noise under the influence of OPD fluctuations exhibits a periodic variation with the increase of the external voltage applied to FPMD1. Specifically, the noise consists of two terms, $\sin(\Delta F)$ and $\sin(2\Delta F)$, as predicted by the theoretical derivation of phase error $\delta\varphi$.

4.3. Effect of OPD noise suppression

To suppress the OPD noise described above, FPMD2 is applied to establish an OPD noise suppression loop, as shown in figure 7. The loop is completed by mixing optical reference phase φ_R and the 1 MHz electrical reference signal φ_0, which is clock synchronized with the AOM driver signal, low-pass filtering, PID controlling, and voltage feedback to FPMD2 through the PZT amplifier. The final detected differential interferometric signal ($\varphi_R - \varphi_M$) is processed in P.M. to reflect the interferometric displacement measurement result.

The corresponding displacement noise amplitude spectrum density (ASD) curve (red curve) is shown in figure 9, in which situation the OPD noise suppression loop is not functioning. To show the suppression effect of the OPD noise suppression loop, the next step is to suppress the system OPD noise based on FPMD2. The phase difference ($\varphi_R - \varphi_0$) is used as an error signal, and the error signal is PID controlled to be zero, which means the optical path of two beams in the reference interferometer is kept the same, i.e. the front-end OPD in the reference interferometer is stabilized at zero. In this case, the displacement noise ASD curve (blue curve) is also shown in figure 9.

As illustrated in figure 9, the displacement noise ASD curve prior to loop locking (red curve) exhibits significantly higher values compared to the post-locking state (blue curve) across the measurement range below 10 mHz. It demonstrates that by stretching or shortening the fiber length of FPMD, the

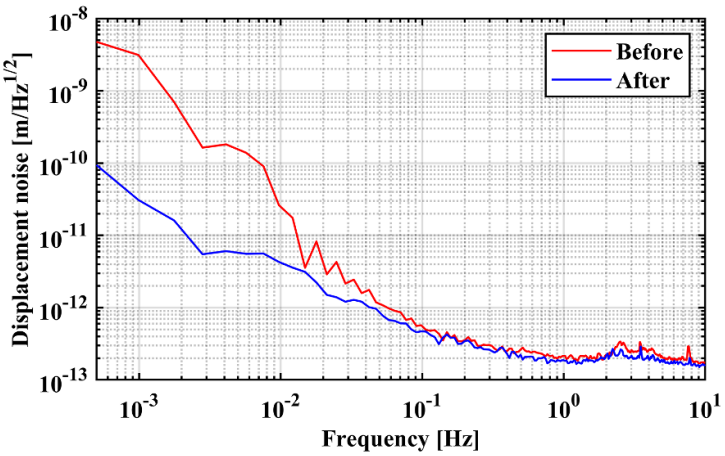

Figure 9. The displacement noise ASD curves.

OPD fluctuation between reference and measurement beams can be compensated via a feedback loop. After the OPD noise suppression, an optimized displacement noise performance is obtained. Specifically, the system attains picometer-level ranging accuracy across the entire frequency band above 2 mHz.

5. Conclusion

This study presents an integrated FPMD to suppress front-end optical path noise in heterodyne interferometry, specifically addressing noise induced by the coupling of sidebands in the AOM. We systematically addressed this problem by: (1) describing the theoretical framework for OPD noise, (2) designing and fabricating a compact FPMD, and (3) validating its noise suppression performance through comprehensive testing. The FPMD demonstrates exceptional performance characteristics, including a highly linear response (270.5949 nm V^{-1}) and significant noise reduction capability in the critical sub-10 mHz frequency range. Experimental results confirm the device's capability to achieve picometer-level ranging accuracy across the entire frequency band above 2 mHz, offering a compact and robust solution for gravitational wave detection and other precision interferometric systems. In the future, a more comprehensive system noise analysis will be conducted, such as the impact of different optical fibers on the noise suppression performance.

Acknowledgment

This paper is supported by the National Key R&D Program of China (Grant Nos. 2021YFC2202902, 2020YFC2200104), the opening project of Key Laboratory of Microgravity, Institute of Mechanics, Chinese Academy of Sciences (Grant No. NML202402).

ORCID iDs

Juan Wang 0009-0005-8992-2961
Keqi Qi 0000-0001-7715-8621
Heshan Liu 0000-0001-9971-1707
Shaoxin Wang 0000-0003-2821-2673
Ziren Luo 0000-0002-9533-8025

References

[1] Bayle J-B, Bonga B, Caprini C, Doneva D, Muratore M, Petiteau A, Rossi E and Shao L 2022 Overview and progress on the Laser Interferometer Space Antenna mission *Nat. Astron.* **6** 1334–8
[2] Luo Z, Wang Y, Wu Y, Hu W and Jin G 2020 The Taiji program: a concise overview *Prog. Theor. Exp. Phys.* **2021** 05A108
[3] Mei J *et al* 2021 The TianQin project: current progress on science and technology *Prog. Theor. Exp. Phys.* **2021** 05A107
[4] Armano M *et al* 2021 Sensor noise in LISA pathfinder: in-flight performance of the optical test mass readout *Phys. Rev. Lett.* **126** 131103
[5] Armano M *et al* 2022 Sensor noise in LISA Pathfinder: an extensive in-flight review of the angular and longitudinal interferometric measurement system *Phys. Rev. D* **106** 082001

[6] Sankar S R and Livas J 2020 Optical alignment and wavefront error demonstration of a prototype LISA telescope *Class. Quantum Gravity* **37** 065005
[7] Steier F 2008 *Interferometry Techniques for Spaceborne Gravitational Wave Detectors* (Leibniz Universität Hannover)
[8] Ming M *et al* 2024 Long-term stability of the picometer-resolution interferometer on TianQin-1 satellite *Class. Quantum Gravity* **41** 165014
[9] Beck M, Chalathadka Subrahmanya S and Gerberding O 2025 Adjustable picometer-stable interferometers for testing space-based gravitational wave detectors *Class. Quantum Gravity* **42** 135001
[10] Heinzel G *et al* 2006 Interferometry for the LISA technology package LTP: an update *J. Phys. Chem.* **32** 132–6
[11] Wand V *et al* 2006 Noise sources in the LTP heterodyne interferometer *Class. Quantum Grav.* **23** S159–S67
[12] Heinzel G, Wand V, Garcia A, Guzman F, Steier F and Killow C J 2008 Investigation of noise sources in the LTP interferometer
[13] Cao B *et al* 2024 Suppression of frequency-mixing effect for pm-level heterodyne interferometers based on "zero coupling" optical path length control *Opt. Lett.* **49** 3300
[14] Monsky A 2010 Understanding interferometric drag-free sensors in space using intelligent data analysis tools
[15] Zhang Y, Hines A S, Valdes G and Guzman F 2021 Investigation and mitigation of noise contributions in a compact heterodyne interferometer *Sensors* **21** 5788
[16] Kittlaus E A, Jones W M, Rakich P T, Otterstrom N T, Muller R E and Rais-Zadeh M 2021 Electrically driven acousto-optics and broadband non-reciprocity in silicon photonics *Nat. Photon.* **15** 43–52
[17] García Marín A F 2007 *Minimisation of Optical Pathlength Noise for the Detection of Gravitational Waves with the Spaceborne Laser Interferometer LISA and LISA Pathfinder* (Leibniz Universität Hannover)
[18] Yang R, Liu H and Luo Z 2024 Optimization design of decimation filter for the phasemeter in the space gravitational wave detection *IEEE Trans. Instrum. Meas.* **73** 1–8
[19] Zhang Q-T, Liu H-S, Dong P, Li P and Luo Z-R 2024 Multi-frequency signal acquisition and phase measurement in space gravitational wave detection *Rev. Sci. Instrum.* **95** 054501
[20] Hechenblaikner G 2013 Common mode noise rejection properties of amplitude and phase noise in a heterodyne interferometer *J. Opt. Soc. Am. A* **30** 941–7
[21] Armano M *et al* 2024 Sensor noise in LISA Pathfinder: Laser frequency noise and its coupling to the optical test mass readout *Phys. Rev. D* **109** 042003
[22] Gerberding O, Isleif K-S, Mehmet M, Danzmann K and Heinzel G 2017 Laser-frequency stabilization via a quasimonolithic Mach-Zehnder interferometer with arms of unequal length and balanced dc readout *Phys. Rev. Appl.* **7** 024027
[23] Smetana J *et al* 2022 Compact Michelson interferometers with subpicometer sensitivity *Phys. Rev. Appl.* **18** 034040